Basic of CFD Coursework: Fluid Mechanics Review and Finite-Difference Prototypes

Jeongbin Jo[1,*]

[1]*Department of Physics, Yonsei University, Seoul, 03722, Republic of Korea*

(Dated: July 10, 2026)

This report collects *Basic of CFD* coursework from HW1 through HW7. HW1 develops analytical fluid-mechanics foundations; HW2–HW5 implement finite-difference prototypes for diffusion (Crank–Nicolson), Poisson relaxation (Jacobi/GS/SOR), Taylor–Green projection on a MAC grid, and lid-driven cavity flow benchmarked against Ghia *et al.* [1] and spin-up histories [2]. HW6 solves the Barenblatt radiative diffusion equation with explicit and implicit Newton schemes and implements a manufactured-solution channel flow with periodic x-boundaries (Pan *et al.* [3]); HW7 extends the projection solver with direct-forcing IBM for cylinder benchmark and oscillating-body flows [4, 5].

CONTENTS

* jeongbin033@yonsei.ac.kr

I. INTRODUCTION

Computational Science and Engineering sits at the intersection of applied mathematics, domain physics, and computing. Its central promise is *predictive simulation*: translate a conservation law or constitutive model into a well-posed boundary-value or initial-value problem, approximate it faithfully on a computer, and validate predictions against exact solutions, asymptotics, or independent experiments. Success depends not only on writing code but on understanding truncation error, stability limits, mesh resolution effects, and the hierarchy of simplified "model problems" that isolate one mathematical difficulty at a time.

Symbolically, one seeks a solution $\mathbf{u}$ in an infinite-dimensional space obeying $\mathcal{L}(\mathbf{u}) = \mathbf{f}$ (possibly nonlinear), then constructs a finite-dimensional approximation $\mathbf{U}_h$ on a mesh with spacing h solving $\mathcal{L}_h(\mathbf{U}_h) = \mathbf{f}_h$. Consistency requires $\|\mathcal{L}_h(\mathbf{R}_h\mathbf{u}) - \mathbf{f}_h\| \to 0$ as $h \to 0$ for a restriction $\mathbf{R}_h$; stability bounds $\|\mathbf{U}_h\|$ in terms of data; convergence $\|\mathbf{U}_h - \mathbf{R}_h\mathbf{u}\| \to 0$ follows when both hold (Lax equivalence for linear problems).

Introductory CFD courses typically progress along that hierarchy: scalar transport and diffusion (parabolic equations), elliptic potentials that arise from implicit steps or streamfunction formulations, divergence-free vector fields and projection operators on staggered meshes, and finally coupled nonlinear dynamics such as incompressible Navier–Stokes flow in benchmark geometries. The homework solutions below follow this progression from analytical review through numerical prototypes.

II. FINITE-DIFFERENCE BUILDING BLOCKS FOR CFD

A. Finite differences and model equations

On a uniform tensor-product mesh with spacing Δx and Δy, second derivatives admit centered three-point stencils with second-order truncation error. For any smooth ψ,

$$\begin{aligned}\delta_{xx}\psi_{i,j} &:= \frac{\psi_{i+1,j} - 2\psi_{i,j} + \psi_{i-1,j}}{(\Delta x)^2} \\ &= \frac{\partial^2\psi}{\partial x^2}(x_i, y_j) + O\big((\Delta x)^2\big), \\ \delta_{yy}\psi_{i,j} &:= \frac{\psi_{i,j+1} - 2\psi_{i,j} + \psi_{i,j-1}}{(\Delta y)^2} \\ &= \frac{\partial^2\psi}{\partial y^2}(x_i, y_j) + O\big((\Delta y)^2\big). \end{aligned} \tag{1}$$

The discrete Laplacian $L_h := \delta_{xx} + \delta_{yy}$ acts on interior nodes; boundary values enter via Dirichlet data or ghost-point extrapolation when Neumann conditions are imposed.

For the heat equation $\partial_t\phi = \alpha\nabla^2\phi + S$, the simplest explicit (forward Euler in time) discretization reads $\phi^{n+1}_{i,j} = \phi^n_{i,j} + \Delta t\big(\alpha(L_h\phi^n)_{i,j} + S^n_{i,j}\big)$. In two dimensions with equal spacing $\Delta x = \Delta y = h$, von Neumann analysis of $\partial_t\phi = \alpha\nabla^2\phi$ yields the stability restriction $\Delta t \le h^2/(4\alpha)$ for this explicit scheme—a quadratic tightening of the timestep relative to mesh refinement.

B. Crank–Nicolson for diffusion

Let L_h denote the five-point Laplacian as above. For $\partial_t\phi = \alpha L_h\phi + S$ with time levels ϕ^n, the Crank–Nicolson (CN) scheme reads

$$\begin{aligned}\frac{\phi^{n+1} - \phi^n}{\Delta t} &= \frac{\alpha}{2}\big(L_h\phi^{n+1} + L_h\phi^n\big) \\ &\quad + \frac{1}{2}\big(S^{n+1} + S^n\big) + O\big((\Delta t)^2\big),\end{aligned} \tag{2}$$

equivalently,

$$\begin{aligned}\big(I - \tfrac{\alpha\Delta t}{2}L_h\big)\phi^{n+1} &= \big(I + \tfrac{\alpha\Delta t}{2}L_h\big)\phi^n \\ &\quad + \frac{\Delta t}{2}\big(S^{n+1} + S^n\big).\end{aligned} \tag{3}$$

For pure diffusion (S=0), amplification-factor analysis of (2) shows $|g| \le 1$ for all Fourier modes when $\alpha\Delta t/h^2 > 0$, i.e. unconditional linear stability of the homogeneous problem; the timestep is then limited by accuracy rather than stability. Each step requires solving a symmetric sparse linear system whose condition number grows as mesh refinement sharpens—often relaxed iteratively instead of factored directly.

C. Iterative elliptic solvers

Consider $L_h u = f$ on interior nodes with $u = g$ on $\partial\Omega$. Writing the five-point stencil as

$$\begin{aligned}&\frac{1}{h^2}\big(u_{i+1,j} + u_{i-1,j} + u_{i,j+1} + u_{i,j-1} - 4u_{i,j}\big) \\ &\quad = f_{i,j},\end{aligned} \tag{4}$$

the Jacobi update isolates $u_{i,j}$,

$$u^{(k+1)}_{i,j} = \frac{1}{4}\Big(u^{(k)}_{i+1,j} + u^{(k)}_{i-1,j} + u^{(k)}_{i,j+1} + u^{(k)}_{i,j-1} - h^2 f_{i,j}\Big), \tag{5}$$

using only values from iteration k. Gauss–Seidel (GS) replaces $u^{(k)}$ by the newest available $u^{(k+1)}$ along the sweep order. Successive Over-Relaxation (SOR) blends the GS correction with the previous iterate:

$$u^{(k+1)}_{i,j} = (1-\omega)\,u^{(k)}_{i,j} + \omega\,u^{\mathrm{GS}}_{i,j}, \qquad \omega \in (1,2)\ \text{(typically)}. \tag{6}$$

The relaxation parameter $\omega > 1$ accelerates convergence relative to GS when chosen near the optimal value for L_h [6, 7]; we use the abbreviation SOR for this method in all homework sections below. Convergence is monitored via the discrete residual $r^{(k)} := L_h u^{(k)} - f$, often reduced in an ℓ^2 norm over interior nodes.

D. Staggered grids and the projection idea

On a MAC grid, scalar quantities live at cell centers $(i + \frac{1}{2}, j + \frac{1}{2})$ while horizontal velocity u sits on vertical edges and vertical velocity v on horizontal edges. A natural discrete divergence at cell $(i + \frac{1}{2}, j + \frac{1}{2})$ is

$$(D_h\mathbf{u})_{i+\frac{1}{2},j+\frac{1}{2}} := \frac{u_{i+1,j+\frac{1}{2}} - u_{i,j+\frac{1}{2}}}{\Delta x} + \frac{v_{i+\frac{1}{2},j+1} - v_{i+\frac{1}{2},j}}{\Delta y}. \tag{7}$$

Given an intermediate velocity $\mathbf{u}^\star$ (after forcing and viscous/convective substeps), one seeks a scalar ϕ such that $\mathbf{u} = \mathbf{u}^\star + \nabla_h \phi$ satisfies $D_h \mathbf{u} = 0$ approximately. Taking D_h of the correction yields the discrete Poisson problem

$$L_h \phi = -D_h \mathbf{u}^\star, \tag{8}$$

with boundary conditions on ϕ consistent with physical boundary data on $\mathbf{u}$ (often homogeneous Neumann on ϕ when normal velocities are prescribed). This is the discrete Helmholtz–Hodge decomposition at the linear algebraic level.

III. VERIFICATION PHILOSOPHY FOR NUMERICAL CFD

Let $\mathbf{u}_h$ be a discrete approximation to $\mathbf{u}$ on N interior degrees of freedom. The global ℓ^2 error (scaled mesh norm)

$$\|\mathbf{e}\|_{2,h} := \left(\frac{1}{N}\sum_{i,j}\left(u_{i,j}^{\text{exact}} - u_{i,j}\right)^2\right)^{1/2} \tag{9}$$

quantifies pointwise agreement when an analytical benchmark exists. For steady cavity flows without closed-form velocity fields, comparison of extracted quantities (centerline velocities, extrema) against independent datasets [1] plays an analogous role.

IV. BCFD HOMEWORK SOLUTIONS

Each subsection follows the problem numbering in the course handouts (HW1–HW7).

A. HW1: Review of fluid mechanics

1. Problem 1: Fluid-mechanics fundamentals

a. Problem. Explain in detail:

(a) density and viscosity;

(b) pressure and flux;

(c) the continuum assumption.

b. Solution.

(a) Density and viscosity. **Density** ρ is the mass per unit volume of a fluid parcel. In continuum mechanics it is treated as a field $\rho(\mathbf{x}, t)$. For a homogeneous incompressible liquid one often takes ρ constant; for gases ρ couples to temperature and pressure through an equation of state (e.g. the ideal gas law). Density enters every conservation law: the mass balance $\partial_t \rho + \nabla \cdot (\rho \mathbf{u}) = 0$ and the inertial terms in the momentum equation.

Viscosity quantifies internal friction—resistance to relative motion of neighboring fluid layers. The *dynamic* (absolute) viscosity μ appears in the Newtonian constitutive relation for the viscous stress tensor,

$$\begin{aligned}\boldsymbol{\tau} = \mu\Big[\nabla\mathbf{u} + (\nabla\mathbf{u})^{\mathsf{T}}\Big]\\ + \lambda(\nabla\cdot\mathbf{u})\,\mathbf{I},\end{aligned} \tag{10}$$

where λ is the second (bulk) viscosity. For an incompressible Newtonian fluid ($\nabla \cdot \mathbf{u} = 0$) the deviatoric stress reduces to $\boldsymbol{\tau} = \mu[\nabla\mathbf{u} + (\nabla\mathbf{u})^{\mathsf{T}}]$, and the viscous force density is $\nabla \cdot \boldsymbol{\tau} = \mu \nabla^2 \mathbf{u}$ when μ is uniform. The *kinematic* viscosity $\nu := \mu/\rho$ has dimensions of diffusivity and appears naturally after dividing the momentum equation by ρ. Viscosity converts kinetic energy into internal energy (heat) through shear; it sets the Reynolds number $\mathrm{Re} = UL/\nu$, which governs whether inertia or viscous diffusion dominates a flow.

(b) Pressure and flux. **Pressure** p is the isotropic part of the Cauchy stress: in a fluid at rest the stress tensor is $-p\mathbf{I}$, so p represents the normal compressive force per unit area exerted on a surface immersed in the fluid. In motion, pressure is defined thermodynamically (for compressible flows) or as the Lagrange multiplier enforcing incompressibility ($\nabla \cdot \mathbf{u} = 0$). It propagates disturbances at the speed of sound in compressible media; in the incompressible limit pressure adjusts instantaneously throughout the domain to satisfy the divergence constraint. Hydrostatic pressure in a gravity field satisfies $\mathrm{d}p/\mathrm{d}z = -\rho g$.

Flux denotes the rate at which a quantity passes through a surface. For mass transport through a surface element $\mathbf{n}\,\mathrm{d}A$, the *mass flux* is $\dot{m} = \int \rho\,\mathbf{u}\cdot\mathbf{n}\,\mathrm{d}A$. More generally, the *convective flux* of a scalar ϕ is $\mathbf{u}\phi$, and the *diffusive flux* (Fick/Fourier analogue) is $-\Gamma\nabla\phi$. In finite-volume CFD one discretizes fluxes through cell faces; their balance over a control volume yields the discrete conservation laws. For incompressible flow the volume flux $\mathbf{u}\cdot\mathbf{n}$ through a closed surface is zero when $\nabla\cdot\mathbf{u} = 0$.

(c) The continuum assumption. Real fluids consist of discrete molecules separated by mean free paths of order ℓ_m. The *continuum hypothesis* replaces this discrete medium by a smooth field defined at every point in space and time, obtained by averaging molecular properties over a *representative elementary volume* (REV) large enough to contain many molecules yet small compared with macroscopic length scales L of the flow geometry.

The dimensionless *Knudsen number* $\mathrm{Kn} = \ell_\mathrm{m}/L$ measures the validity of this picture: when $\mathrm{Kn} \ll 1$, collisions equilibrate molecules locally and continuum fields (ρ, $\mathbf{u}$, p, T) vary smoothly on scale L. When $\mathrm{Kn} \sim 1$ or larger—rarefied gases, micro-scale flows, or very low pressures—molecular discreteness matters and kinetic theory or direct simulation (DSMC) replaces the Navier–Stokes equations.

Under the continuum assumption, conservation of mass, momentum, and energy hold for any control volume, and constitutive relations (Newtonian viscosity, Fourier heat conduction, etc.) link fluxes to gradients of state variables. All CFD discretizations in this course inherit this assumption: grid spacing h must satisfy $\ell_\mathrm{m} \ll h \ll L$ so that each computational cell contains a valid continuum average while resolving the macroscopic flow.

2. Problem 2: Incompressible Navier–Stokes in cylindrical coordinates

a. Problem. Derive the incompressible Navier–Stokes equations in cylindrical coordinates (r, θ, z) using a control-volume approach.

b. Solution.

Control volume and kinematics. Consider a fixed control volume (CV) bounded by $r \in [r, r + \Delta r]$, $\theta \in [\theta, \theta + \Delta\theta]$, and

$z \in [z, z+\Delta z]$. The volume and face areas are

$$\begin{aligned} \Delta V &= r\,\Delta r\,\Delta\theta\,\Delta z, \\ A_r &= r\,\Delta\theta\,\Delta z, \quad A_\theta = \Delta r\,\Delta z, \quad A_z = r\,\Delta r\,\Delta\theta, \end{aligned} \tag{11}$$

with outward unit normals $\mathbf{e}_r$, $\mathbf{e}_\theta$, $\mathbf{e}_z$. The velocity is $\mathbf{u} = u_r\mathbf{e}_r + u_\theta\mathbf{e}_\theta + u_z\mathbf{e}_z$. For an incompressible Newtonian fluid with constant density ρ and dynamic viscosity μ, Reynolds transport on the CV gives, for any vector field $\boldsymbol{\Psi}$,

$$\begin{aligned} &\frac{\mathrm{d}}{\mathrm{d}t}\int_{CV}\rho\boldsymbol{\Psi}\,\mathrm{d}V = \int_{CV}\rho\,\frac{D\boldsymbol{\Psi}}{Dt}\,\mathrm{d}V \\ &= -\oint_{\partial CV}\rho(\mathbf{u}\cdot\mathbf{n})\,\boldsymbol{\Psi}\,\mathrm{d}A + \int_{CV}\rho\,\mathbf{f}\,\mathrm{d}V + \oint_{\partial CV}\mathbf{t}\,\mathrm{d}A, \end{aligned} \tag{12}$$

where $\mathbf{f}$ is a body force per unit mass and $\mathbf{t} = \boldsymbol{\sigma}\cdot\mathbf{n}$ is the surface traction with Cauchy stress $\boldsymbol{\sigma} = -p\mathbf{I} + \boldsymbol{\tau}$,

$$\boldsymbol{\tau} = \mu\big[\nabla\mathbf{u} + (\nabla\mathbf{u})^{\mathsf{T}}\big]. \tag{13}$$

Mass conservation (continuity). Take $\boldsymbol{\Psi} = \mathbf{1}$ in the flux term of (12). With no mass source,

$$0 = -\oint_{\partial CV}\rho\,\mathbf{u}\cdot\mathbf{n}\,\mathrm{d}A. \tag{14}$$

Balancing fluxes through the six faces and dividing by ΔV as $\Delta r, \Delta\theta, \Delta z \to 0$ yields

$$\frac{1}{r}\frac{\partial(ru_r)}{\partial r} + \frac{1}{r}\frac{\partial u_\theta}{\partial\theta} + \frac{\partial u_z}{\partial z} = 0, \tag{15}$$

the incompressible continuity equation in cylindrical coordinates. The factors $1/r$ arise because the r-face area grows linearly with r while arc length in θ scales as $r\,\Delta\theta$.

r-momentum balance. Set $\boldsymbol{\Psi} = u_r\mathbf{e}_r$ in (12). The local time rate is $\rho\,\partial u_r/\partial t\,\Delta V$ to leading order. Convective flux through the r-faces contributes

$$\begin{aligned} &\big[(r+\Delta r)(u_r\big|_{r+\Delta r})^2 - r(u_r\big|_r)^2\big]\Delta\theta\,\Delta z \\ &\longrightarrow \frac{\partial(ru_r^2)}{\partial r}\,\Delta\theta\,\Delta z, \end{aligned} \tag{16}$$

which, combined with θ- and z-face fluxes and division by $\Delta V = r\,\Delta r\,\Delta\theta\,\Delta z$, produces the r-convection group

$$u_r\frac{\partial u_r}{\partial r} + \frac{u_\theta}{r}\frac{\partial u_r}{\partial\theta} + u_z\frac{\partial u_r}{\partial z} - \frac{u_\theta^2}{r}. \tag{17}$$

The last term $-u_\theta^2/r$ is the centrifugal contribution: as fluid moves in θ, the unit vector $\mathbf{e}_r$ rotates, so transport of r-momentum through the curved θ-faces introduces this source-like term even in steady flow.

Pressure and body-force volume integrals give $-\partial p/\partial r$ and ρf_r. Summing viscous traction over the six faces and taking the limit gives the Laplacian form below. Collecting terms, the r-momentum equation is

$$\begin{aligned} &\frac{\partial u_r}{\partial t} + u_r\frac{\partial u_r}{\partial r} + \frac{u_\theta}{r}\frac{\partial u_r}{\partial\theta} + u_z\frac{\partial u_r}{\partial z} - \frac{u_\theta^2}{r} \\ &= -\frac{1}{\rho}\frac{\partial p}{\partial r} + \nu\nabla^2 u_r - \nu\frac{u_r}{r^2} - \frac{2\nu}{r^2}\frac{\partial u_\theta}{\partial\theta} + f_r, \end{aligned} \tag{18}$$

where $\nu = \mu/\rho$ and

$$\nabla^2 u_r := \frac{1}{r}\frac{\partial}{\partial r}\left(r\frac{\partial u_r}{\partial r}\right) + \frac{1}{r^2}\frac{\partial^2 u_r}{\partial\theta^2} + \frac{\partial^2 u_r}{\partial z^2}. \tag{19}$$

θ- and z-momentum. The same flux balance on the θ-faces generates a Coriolis-like coupling $+u_r u_\theta/r$ in the θ-momentum equation, and the pressure gradient appears with a $1/r$ geometric factor:

$$\begin{aligned} &\frac{\partial u_\theta}{\partial t} + u_r\frac{\partial u_\theta}{\partial r} + \frac{u_\theta}{r}\frac{\partial u_\theta}{\partial\theta} + u_z\frac{\partial u_\theta}{\partial z} + \frac{u_r u_\theta}{r} \\ &= -\frac{1}{\rho r}\frac{\partial p}{\partial\theta} + \nu\nabla^2 u_\theta - \nu\frac{u_\theta}{r^2} + \frac{2\nu}{r^2}\frac{\partial u_r}{\partial\theta} + f_\theta, \end{aligned} \tag{20}$$

with $\nabla^2 u_\theta$ defined analogously to (18). Because the z-direction is Cartesian within the (r,θ) plane, no curvature correction appears in the convective term:

$$\begin{aligned} &\frac{\partial u_z}{\partial t} + u_r\frac{\partial u_z}{\partial r} + \frac{u_\theta}{r}\frac{\partial u_z}{\partial\theta} + u_z\frac{\partial u_z}{\partial z} \\ &= -\frac{1}{\rho}\frac{\partial p}{\partial z} + \nu\nabla^2 u_z + f_z, \end{aligned} \tag{21}$$

where

$$\nabla^2 u_z = \frac{1}{r}\frac{\partial}{\partial r}\left(r\frac{\partial u_z}{\partial r}\right) + \frac{1}{r^2}\frac{\partial^2 u_z}{\partial\theta^2} + \frac{\partial^2 u_z}{\partial z^2}. \tag{22}$$

Vector form. Equations (15)–(21) are equivalent to

$$\nabla\cdot\mathbf{u} = 0, \qquad \frac{\partial\mathbf{u}}{\partial t} + (\mathbf{u}\cdot\nabla)\mathbf{u} = -\frac{1}{\rho}\nabla p + \nu\nabla^2\mathbf{u} + \mathbf{f}, \tag{23}$$

provided the cylindrical operators $(\mathbf{u}\cdot\nabla)$, ∇p, and $\nabla^2\mathbf{u}$ are expanded in (r,θ,z); the extra $-u_\theta^2/r$ and $\pm u_r u_\theta/r$ terms in (17) and (20) are precisely the metric contributions that distinguish curvilinear control-volume balances from their Cartesian counterpart.

3. *Problem 3: Film flow on an inclined plane*

a. Problem. Consider laminar flow of a fluid layer of thickness h falling down a plane inclined at angle θ to the horizontal (fully developed, x along the free surface, y normal toward the wall, gravity g, kinematic viscosity ν).

(a) Show that

$$u(y) = \tfrac{g}{2\nu}(h^2 - y^2)\sin\theta. \tag{24}$$

(b) Show that the volume flow rate per unit width is

$$Q = \tfrac{gh^3}{3\nu}\sin\theta. \tag{25}$$

(c) Show that the wall frictional stress is

$$\tau_0 = \rho g h\sin\theta, \tag{26}$$

where ρ is fluid density.

b. Solution.

Governing equation and boundary conditions. Take $y = 0$ at the free surface and $y = h$ at the wall (y increases toward the plane). Fully developed laminar flow has $u = u(y)$ only, $v = 0$, and $\partial u/\partial x = 0$. The x-momentum equation reduces to

$$0 = -\frac{1}{\rho}\frac{\partial p}{\partial x} + g\sin\theta + \nu\frac{\mathrm{d}^2 u}{\mathrm{d}y^2}, \tag{27}$$

where $g\sin\theta$ is the downslope component of gravitational acceleration. At the free surface the gauge pressure is constant, so $\partial p/\partial x = 0$ throughout the film. Hence

$$\frac{\mathrm{d}^2 u}{\mathrm{d}y^2} = -\frac{g\sin\theta}{\nu}. \tag{28}$$

The free surface carries no external tangential stress, so $\mathrm{d}u/\mathrm{d}y = 0$ at $y = 0$; the wall is no-slip, so $u = 0$ at $y = h$.

(a) Velocity profile. Integrating (28) twice and applying the boundary conditions,

$$\frac{\mathrm{d}u}{\mathrm{d}y} = -\frac{g\sin\theta}{\nu}\,y, \qquad u(y) = -\frac{g\sin\theta}{2\nu}\,y^2 + C. \tag{29}$$

Imposing $u(h) = 0$ gives $C = (g\sin\theta/(2\nu))h^2$, therefore

$$u(y) = \frac{g\sin\theta}{2\nu}\,(h^2 - y^2). \tag{30}$$

The profile is parabolic with maximum speed $u_{\max} = gh^2\sin\theta/(2\nu)$ at the free surface ($y = 0$) and zero at the wall.

(b) Volume flow rate per unit width. Integrating across the film thickness,

$$\begin{aligned} Q &= \int_0^h u(y)\,\mathrm{d}y = \frac{g\sin\theta}{2\nu}\int_0^h (h^2 - y^2)\,\mathrm{d}y \\ &= \frac{g\sin\theta}{2\nu}\left[h^2 y - \frac{y^3}{3}\right]_0^h = \frac{g\sin\theta}{2\nu}\left(h^3 - \frac{h^3}{3}\right) = \frac{gh^3\sin\theta}{3\nu}. \end{aligned} \tag{31}$$

(c) Wall frictional stress. The Newtonian shear stress is $\tau = \mu\,\mathrm{d}u/\mathrm{d}y$. At the wall ($y = h$),

$$\left.\frac{\mathrm{d}u}{\mathrm{d}y}\right|_{y=h} = -\frac{gh\sin\theta}{\nu}, \tag{32}$$

so the magnitude of the frictional stress exerted by the fluid on the wall is

$$\tau_0 = \mu\left|\frac{\mathrm{d}u}{\mathrm{d}y}\right|_{y=h} = \rho\nu\,\frac{gh\sin\theta}{\nu} = \rho g h\sin\theta. \tag{33}$$

Physically, this equals the component of the film weight per unit area parallel to the plane: a force balance on the control volume confirms that wall shear supports the downslope weight of the layer in steady flow.

4. *Problem 4: Steady laminar annular flow*

a. Problem. Steady laminar axial flow occupies the annulus between coaxial tubes of inner radius a and outer radius b, driven by pressure gradient $\mathrm{d}p/\mathrm{d}z$.

(a) Find the axial velocity $u_z(r)$.

(b) Find the radius of maximum velocity.

(c) Find the volume flow rate.

b. Solution.

Governing equation. Fully developed steady axial flow has $u_z = u(r)$ only. With constant $\mathrm{d}p/\mathrm{d}z < 0$, the z-momentum equation reduces to

$$0 = \frac{1}{\rho}\frac{\mathrm{d}p}{\mathrm{d}z} + \nu\,\frac{1}{r}\frac{\mathrm{d}}{\mathrm{d}r}\left(r\frac{\mathrm{d}u_z}{\mathrm{d}r}\right). \tag{34}$$

Define $G := -\mathrm{d}p/\mathrm{d}z/(\rho\nu) > 0$. Then

$$\frac{1}{r}\frac{\mathrm{d}}{\mathrm{d}r}\left(r\frac{\mathrm{d}u_z}{\mathrm{d}r}\right) = G, \qquad \frac{\mathrm{d}}{\mathrm{d}r}\left(r\frac{\mathrm{d}u_z}{\mathrm{d}r}\right) = Gr. \tag{35}$$

Integrating twice,

$$\frac{\mathrm{d}u_z}{\mathrm{d}r} = \frac{Gr}{2} + \frac{C_1}{r}, \qquad u_z(r) = \frac{Gr^2}{4} + C_1\ln r + C_2. \tag{36}$$

(a) Velocity profile. No-slip at $r = a$ and $r = b$ gives

$$\frac{Ga^2}{4} + C_1\ln a + C_2 = 0, \qquad \frac{Gb^2}{4} + C_1\ln b + C_2 = 0. \tag{37}$$

Subtracting and solving for C_1, C_2,

$$u_z(r) = \frac{G}{4}\left[(r^2 - a^2) - \frac{b^2 - a^2}{\ln(b/a)}\ln\frac{r}{a}\right], \qquad G = -\frac{1}{\rho\nu}\frac{\mathrm{d}p}{\mathrm{d}z}. \tag{38}$$

(b) Radius of maximum velocity. Differentiating and setting $\mathrm{d}u_z/\mathrm{d}r = 0$,

$$2r - \frac{b^2 - a^2}{r\,\ln(b/a)} = 0 \quad\Longrightarrow\quad r_{\max} = \sqrt{\frac{b^2 - a^2}{2\ln(b/a)}}. \tag{39}$$

Provided $a < r_{\max} < b$, the peak lies in the annulus (not on either wall).

(c) Volume flow rate. The volumetric flow rate is $Q = 2\pi\int_a^b u_z(r)\,r\,\mathrm{d}r$. Using the profile above,

$$\begin{aligned} Q &= \frac{\pi G}{2}\int_a^b \left[r(r^2 - a^2) - \frac{b^2 - a^2}{\ln(b/a)}\,r\ln\frac{r}{a}\right]\mathrm{d}r \\ &= \frac{\pi G}{8}\left[\frac{(b^2 - a^2)^2}{\ln(b/a)} - (b^2 - a^2)(b^2 + a^2)\right]. \end{aligned} \tag{40}$$

Equivalently,

$$\begin{aligned} Q &= \frac{\pi(b^2 - a^2)}{8\mu}\left(-\frac{\mathrm{d}p}{\mathrm{d}z}\right) \\ &\quad\times\left[\frac{b^2 - a^2}{\ln(b/a)} - (b^2 + a^2)\right], \qquad \mu = \rho\nu. \end{aligned} \tag{41}$$

When $a \to 0$, this recovers the Hagen–Poiseuille result $Q = \pi b^4(-\mathrm{d}p/\mathrm{d}z)/(8\mu)$.

5. *Problem 5: Unsteady channel flow with harmonic forcing*

a. Problem. In an infinitely long channel of height h, unsteady laminar flow is driven by a harmonic pressure gradient

$$-\frac{1}{\rho}\frac{\partial p}{\partial x} = K\sin\omega t, \tag{42}$$

with $u = 0$ at $y = \pm h/2$ and motion independent of x.

(a) Find $u(y, t)$.

(b) Asymptotic formula as $\omega \to 0$.

(c) Asymptotic formula as $\omega \to \infty$.

(d) Discuss the effect of forcing frequency ω.

b. Solution.

Governing equation. With $u = u(y,t)$, $\partial_x u = 0$, and no body force,

$$\frac{\partial u}{\partial t} = \nu \frac{\partial^2 u}{\partial y^2} + K \sin \omega t, \qquad u\left(\pm\frac{h}{2}, t\right) = 0. \tag{43}$$

(a) Velocity $u(y,t)$. Seek a harmonic response $u = \Re\{U(y)\,\mathrm{e}^{\mathrm{i}\omega t}\}$. Substituting into (43),

$$U'' - \lambda^2 U = -\frac{K}{\nu}, \qquad \lambda^2 := \frac{\mathrm{i}\omega}{\nu} = (1+\mathrm{i})^2\,\frac{\omega}{2\nu}. \tag{44}$$

The solution with even symmetry about $y = 0$ is

$$U(y) = \frac{\mathrm{i}K}{\omega}\left[\frac{\cosh(\lambda y)}{\cosh(\lambda h/2)} - 1\right], \tag{45}$$

which satisfies $U(\pm h/2) = 0$. The real velocity is

$$u(y,t) = \Re\{U(y)\,\mathrm{e}^{\mathrm{i}\omega t}\} = \frac{K}{\omega}\,\Im\left\{\left[\frac{\cosh(\lambda y)}{\cosh(\lambda h/2)} - 1\right]\mathrm{e}^{\mathrm{i}\omega t}\right\}. \tag{46}$$

Writing $\lambda = (1+\mathrm{i})k$ with $k = \sqrt{\omega/(2\nu)}$, the hyperbolic functions split into real and imaginary parts; the amplitude grows toward the channel center when ω is small and collapses into wall layers when ω is large.

(b) Slow oscillation ($\omega \to 0$). When the forcing period is long, inertia is negligible at leading order and (43) reduces to the quasi-steady balance

$$0 = \nu \frac{\partial^2 u}{\partial y^2} + K \sin \omega t. \tag{47}$$

Integrating with $u(\pm h/2) = 0$ gives

$$u(y,t) = \frac{K \sin \omega t}{2\nu}\left[\left(\frac{h}{2}\right)^2 - y^2\right] = \frac{K \sin \omega t}{2\nu}\left(\frac{h^2}{4} - y^2\right). \tag{48}$$

This is instantaneous Poiseuille flow driven by the slowly varying pressure gradient.

(c) Fast oscillation ($\omega \to \infty$). Define the viscous penetration depth $\delta = \sqrt{2\nu/\omega} \to 0$. Then $|\lambda h| \gg 1$, $\cosh(\lambda y)/\cosh(\lambda h/2)$ is appreciable only within $O(\delta)$ of the walls. In the channel interior $|y| \lesssim h/2 - O(\delta)$,

$$u(y,t) \approx 0, \tag{49}$$

while near each wall the flow oscillates in thin Stokes layers with amplitude $\propto K/\omega$. High-frequency forcing cannot penetrate far from the boundaries before viscous diffusion attenuates it.

(d) Effect of forcing frequency ω. The parameter $kh = \sqrt{\omega/(2\nu)}\,h$ measures channel height in units of the penetration depth. For $kh \ll 1$ (low ω), the parabolic profile of part (b) is recovered across the full gap. For $kh \gg 1$ (high ω), plug-flow-like cores with wall layers dominate and the peak speed scales as K/ω. Between these limits the complex ratio $\cosh(\lambda y)/\cosh(\lambda h/2)$ introduces phase lag between u and the pressure forcing: fluid near the walls responds first, and the center lags as ω increases.

B. HW2: Heat equations

1. Problem 1: Exact steady-state solution

a. Problem. On $\Omega = [-1,1]^2$, solve the heat equation with source $S(x,y) = 2(2 - x^2 - y^2)$, $\alpha = 1$, and homogeneous initial and boundary data. Find the exact ϕ at steady state.

b. Theory. The transient conduction–source model

$$\frac{\partial \phi}{\partial t} = \alpha \nabla^2 \phi + S(\mathbf{x}), \qquad \phi|_{\partial\Omega} = 0, \quad \phi(\cdot, 0) = 0 \tag{50}$$

describes a diffusing scalar driven toward equilibrium by diffusion and volumetric forcing [7]. At steady state $\partial_t \phi = 0$, the field satisfies the elliptic problem $\nabla^2\phi = -S/\alpha$ with the same boundary data—the limit approached by the time-marching scheme in Problems 2–3.

c. Solution. With $\alpha = 1$ and $S(x,y) = 2(2 - x^2 - y^2)$, the exact steady solution is $\phi_{\text{exact}} = (1-x^2)(1-y^2)$, since

$$\frac{\partial^2 \phi_{\text{exact}}}{\partial x^2} = -2(1-y^2), \tag{51}$$

$$\frac{\partial^2 \phi_{\text{exact}}}{\partial y^2} = -2(1-x^2), \tag{52}$$

$$\nabla^2 \phi_{\text{exact}} = -4 + 2x^2 + 2y^2 = -S(x,y). \tag{53}$$

Boundary data vanish because $1 - x^2$ or $1 - y^2$ is zero on each side of the square.

2. Problem 2: Crank–Nicolson numerical solution

a. Problem. Using Crank–Nicolson time advancement and second-order central differences in space, march (50) to steady state on a uniform grid. Plot the exact and numerical steady solutions.

b. Theory. On a uniform grid with spacing h and five-point Laplacian L_h (Sec. II), the CN scheme [6, 8] for (50) reads

$$\frac{\phi^{n+1} - \phi^n}{\Delta t} = \frac{\alpha}{2}\left(L_h\phi^{n+1} + L_h\phi^n\right) + S, \tag{54}$$

where S is evaluated at grid nodes and held fixed in time. Rearranging,

$$\left(I - \tfrac{\alpha\Delta t}{2} L_h\right)\phi^{n+1} = \left(I + \tfrac{\alpha\Delta t}{2} L_h\right)\phi^n + \Delta t\, S. \tag{55}$$

Each time step requires an elliptic solve; CN is unconditionally stable for the model diffusion operator and second-order accurate in Δt [6].

c. Solution. The C++ driver `hw2_heat` implements (55) on $[-1,1]^2$:

- $\alpha = 1$; $N = 64$ intervals per direction ($h = 2/N$); $\Delta t = 0.01$;
- five-point L_h and analytic $S(x,y) = 2(2 - x^2 - y^2)$ at interior nodes;
- $r = \alpha\Delta t/(2h^2)$; each CN step solved by successive over-relaxation (SOR; Sec. II, Eq. (6)) with $\omega = 1.7$, up to 80 sweeps, inner tolerance 10^{-12}) using the update

$$\phi_{i,j}^{n+1} \leftarrow (1-\omega)\,\phi_{i,j}^{n+1} + \omega\,\frac{\mathrm{RHS}_{i,j} + r\sum_{\text{neighbors}}\phi^{n+1}}{1+4r}; \tag{56}$$

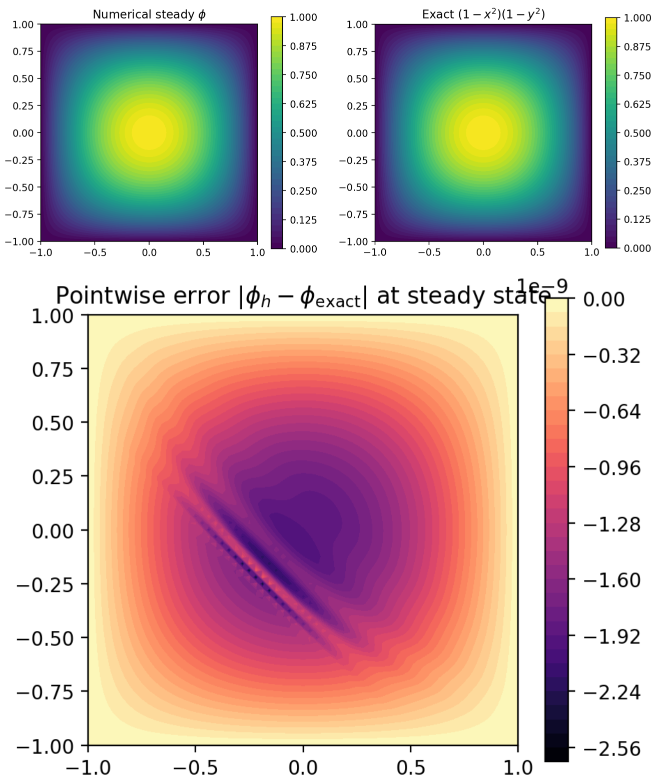

FIG. 1. Problem 2 ($N = 64$, $\Delta t = 0.01$): numerical steady ϕ_h, exact $\phi_{\text{exact}} = (1 - x^2)(1 - y^2)$, and absolute error.

- time marching stops when $\|\phi^{n+1} - \phi^n\|_\infty < 10^{-10}$ (step 407 for the default run).

Interior ℓ^2 error against ϕ_{exact} is 9.8×10^{-10}. Figure 1 shows the numerical steady field, the exact surface, and pointwise $|\phi_h - \phi_{\text{exact}}|$.

3. *Problem 3: Order of accuracy*

a. Problem. Discuss the order of accuracy in time and space based on numerical results.

b. Theory. Truncation analysis gives $O(\Delta t^2)$ for CN and $O(h^2)$ for centered differences [6, 8]. Empirical orders follow

$$p \approx \frac{\log(e_1/e_2)}{\log(r_1/r_2)}, \tag{57}$$

where r denotes Δt or h.

c. Solution.

Spatial refinement. Table I lists interior ℓ^2 error after steady state with $\Delta t = 10^{-3}$ (temporal error negligible). Errors stay near 10^{-8}–10^{-9} for all N.

Because $\phi_{\text{exact}} = (1 - x^2)(1 - y^2)$ is biquadratic, the three-point second difference is exact along each coordinate on a uniform mesh, so the five-point L_h also annihilates ϕ_{exact} with the given S [6]. Spatial truncation therefore does not appear in this manufactured solution; only time-stepping bias and solver tolerances remain.

Temporal refinement. Fixing $N = 64$ and varying Δt isolates CN time error (Table II, Figure 2). For $\Delta t = 0.08$ and 0.04 (above the tolerance floor), halving Δt reduces error by $\sim 470\times$, giving an effective order $p \approx 8.9$—larger than two because large steps bias the transient toward steady state. Once $\Delta t \le 0.02$, errors saturate near 10^{-10}, set by SOR and steady-monitor tolerances.

TABLE I. Spatial refinement ($\Delta t = 10^{-3}$, `hw2_heat`).

N	$h = 2/N$	$\|\phi_h - \phi_{\text{exact}}\|_{2,h}$
8	0.250	1.17×10^{-8}
16	0.125	1.08×10^{-8}
32	0.0625	1.04×10^{-8}
64	0.03125	1.03×10^{-8}
128	0.015625	1.01×10^{-8}

TABLE II. Temporal refinement ($N = 64$, `hw2_heat`).

Δt	steady step	$\|\phi_h - \phi_{\text{exact}}\|_{2,h}$
0.08	998	1.66×10^{-3}
0.04	499	3.56×10^{-6}
0.02	249	1.43×10^{-10}
0.01	407	9.78×10^{-10}
0.005	786	2.00×10^{-9}

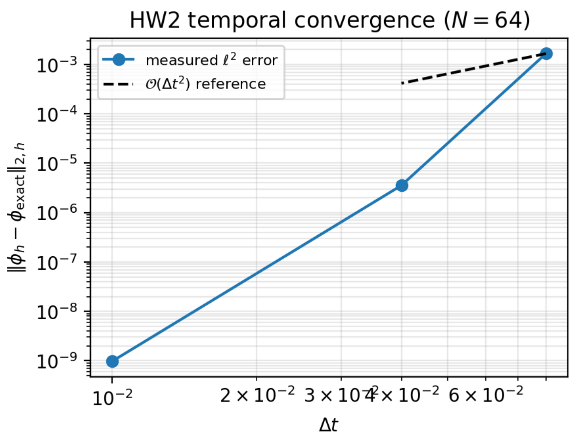

FIG. 2. Problem 3: measured ℓ^2 error vs. Δt ($N = 64$); dashed line shows $O(\Delta t^2)$ reference anchored at $\Delta t = 0.08$. Points below $\sim 10^{-10}$ lie on the solver tolerance floor.

Summary. The `hw2_heat` results confirm agreement with the analytical steady field (Problem 1) and second-order CN design in time before numerical floors dominate. Spatial order is not observable for this particular ϕ_{exact}; a non-polynomial steady solution would be needed to expose $O(h^2)$ spatial convergence.

TABLE III. Problem 1: Jacobi, Gauss–Seidel, and SOR ($N = 64$, tol. 10^{-8}).

Method	Iterations	Wall time (s)	$\|u - u_{\text{exact}}\|_{2,h}$
Jacobi	14 722	0.90	5.17×10^{-6}
Gauss–Seidel	7 362	0.44	5.17×10^{-6}
SOR ($\omega = 1.85$)	550	0.033	5.17×10^{-6}

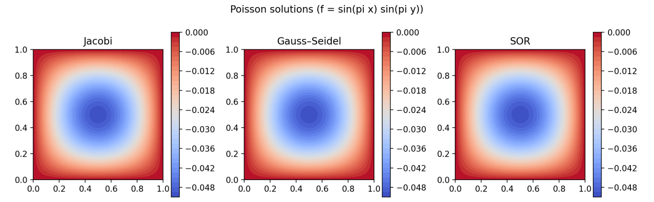

FIG. 3. Problem 1: discrete solutions from Jacobi, Gauss–Seidel, and SOR ($f = \sin \pi x \, \sin \pi y$).

C. HW3: Poisson equations

1. Problem 1: Iterative Poisson solver

a. Problem. On $[0, 1]^2$ solve $\nabla^2 u = f$ with $u|_{\partial\Omega} = 0$ and $f(x, y) = \sin(\pi x) \sin(\pi y)$.

(1) Develop Jacobi, Gauss–Seidel, and SOR solvers on a uniform five-point grid.

(2) Compare iteration counts, residuals, and errors.

b. Theory. The Poisson problem with homogeneous Dirichlet data is the elliptic limit of diffusion with fixed source [7]. On a uniform grid with spacing $h = 1/N$, the five-point Laplacian L_h and iterative updates (Jacobi, Gauss–Seidel, successive over-relaxation) are given in Sec. II. Convergence is monitored by the interior ℓ^2 residual $\|L_h u^{(k)} - f\|_{2,h}$.

For $f = \sin(\pi x) \sin(\pi y)$, the continuous eigenfunction relation

$$\nabla^2 \big(\sin \pi x \, \sin \pi y \big) = -2\pi^2 \sin \pi x \, \sin \pi y \tag{58}$$

yields the exact solution $u_{\text{exact}} = -(2\pi^2)^{-1} \sin(\pi x) \sin(\pi y)$.

c. Solution. The driver `hw3_poisson` discretizes $[0, 1]^2$ with $N = 64$, applies each method until $\|L_h u - f\|_{2,h} < 10^{-8}$, and records wall time and ℓ^2 error against u_{exact}. SOR uses $\omega = 1.85$.

All three methods converge to the same discrete solution; GS halves Jacobi iterations by using updated neighbors immediately, and SOR accelerates GS further [6]. The $O(h^2)$ spatial error ($h = 1/64$) dominates the reported ℓ^2 mismatch with the analytic field. Figure 3–4 show the discrete fields and iteration counts.

2. Problem 2: Linearity

a. Problem. On $[0, 1]^2$ with $u = 0$ on $\partial\Omega$, solve $\nabla^2 u = f_1 + f_2$ where

$$f_1(x, y) = \sin(\pi x) \sin(\pi y), \tag{59}$$

$$f_2(x, y) = \exp\big(- 100((x - 0.5)^2 + (y - 0.5)^2) \big). \tag{60}$$

(1) Find u for $f_1 + f_2$ using SOR.

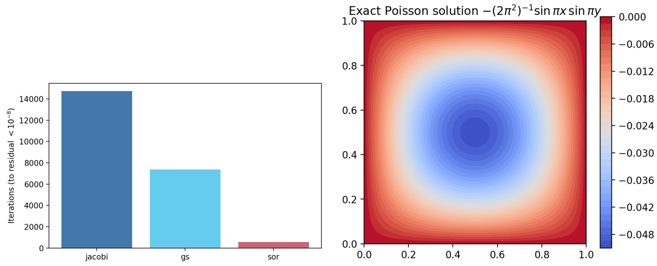

FIG. 4. Problem 1: iteration counts to residual 10^{-8} (left) and exact field (right).

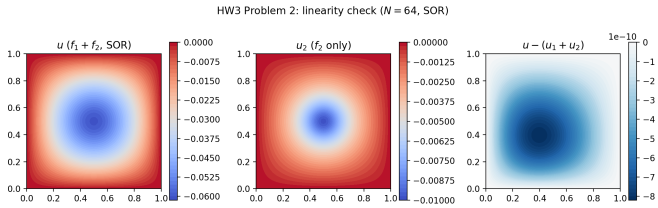

FIG. 5. Problem 2: combined solution u, localized u_2, and superposition error $u - (u_1 + u_2)$ ($N = 64$, SOR).

(2) Find u_2 for forcing f_2 only.

(3) Compare u with $u_1 + u_2$, where u_1 is the Problem 1 SOR solution for f_1.

b. Theory. Poisson's equation with fixed Dirichlet data is linear: if $\nabla^2 u_1 = f_1$ and $\nabla^2 u_2 = f_2$, then $\nabla^2(u_1 + u_2) = f_1 + f_2$. The same superposition holds for the discrete system $L_h u = f$ because L_h is linear [6]. Numerically, u_h from SOR with $f_1 + f_2$ should agree with $u_{1,h} + u_{2,h}$ up to solver tolerance (and any boundary-discretization bias, which vanishes here because $u = 0$ is imposed exactly on the grid boundary).

c. Solution. Using the same grid ($N = 64$), SOR ($\omega = 1.85$), and residual tolerance 10^{-8}:

- u (combined forcing): 553 iterations, 0.040 s;
- u_2 (f_2 only): 485 iterations, 0.012 s;
- u_1 is reused from Problem 1 SOR (550 iterations for f_1 alone).

The interior ℓ^∞ norm $\|u - (u_1 + u_2)\|_\infty$ is 8.2×10^{-10}, at the level of the SOR stopping criterion. Figure 5 shows u, the localized u_2 from the Gaussian f_2, and the superposition defect $u - (u_1 + u_2)$.

The defect is negligible compared with the $O(10^{-6})$ discretization error in Problem 1, confirming that the five-point Poisson discretization and SOR implementation preserve linearity as expected.

D. HW4: Taylor–Green vortex

1. Problem 1: Exact solution

a. Problem. On $0 \le x, y \le 2\pi$, the Taylor–Green vortex is given by

$$\begin{aligned} u(x,y,t) &= \sin x\, \cos y\, F(t), \\ v(x,y,t) &= -\cos x\, \sin y\, F(t), \\ p(x,y,t) &= \tfrac{\rho}{4}\big(\cos 2x + \cos 2y\big)\, F^2(t), \\ F(t) &= e^{-2\nu t}, \end{aligned} \tag{61}$$

with kinematic viscosity ν and density ρ. Verify that (u, v, p) satisfies the incompressible Navier–Stokes equations.

b. Theory. For constant ρ, the incompressible Navier–Stokes system in two dimensions is [6, 7]

$$\frac{\partial u}{\partial x} + \frac{\partial v}{\partial y} = 0, \tag{62}$$

$$\frac{\partial u}{\partial t} + u\frac{\partial u}{\partial x} + v\frac{\partial u}{\partial y} = -\frac{1}{\rho}\frac{\partial p}{\partial x} + \nu\left(\frac{\partial^2 u}{\partial x^2} + \frac{\partial^2 u}{\partial y^2}\right), \tag{63}$$

$$\frac{\partial v}{\partial t} + u\frac{\partial v}{\partial x} + v\frac{\partial v}{\partial y} = -\frac{1}{\rho}\frac{\partial p}{\partial y} + \nu\left(\frac{\partial^2 v}{\partial x^2} + \frac{\partial^2 v}{\partial y^2}\right). \tag{64}$$

Verification requires substituting the ansatz, computing every derivative, and showing that (62)–(64) hold identically provided $F' = -2\nu F$.

c. Solution.

Step 1: partial derivatives. Because F depends only on t,

$$\begin{aligned} \frac{\partial u}{\partial t} &= \sin x\, \cos y\, F', \\ \frac{\partial v}{\partial t} &= -\cos x\, \sin y\, F', \\ \frac{\partial u}{\partial x} &= \cos x\, \cos y\, F, \\ \frac{\partial u}{\partial y} &= -\sin x\, \sin y\, F, \\ \frac{\partial v}{\partial x} &= \sin x\, \sin y\, F, \\ \frac{\partial v}{\partial y} &= -\cos x\, \cos y\, F, \\ \frac{\partial^2 u}{\partial x^2} = \frac{\partial^2 u}{\partial y^2} &= -\sin x\, \cos y\, F, \\ \frac{\partial^2 v}{\partial x^2} = \frac{\partial^2 v}{\partial y^2} &= \cos x\, \sin y\, F. \end{aligned} \tag{65}$$

Hence

$$\begin{aligned} \nabla^2 u &= -2\sin x\, \cos y\, F = -2u, \\ \nabla^2 v &= 2\cos x\, \sin y\, F = -2v. \end{aligned} \tag{66}$$

For pressure, using $\partial_x \cos 2x = -2\sin 2x = -4\sin x\cos x$ (and similarly in y),

$$\begin{aligned} \frac{\partial p}{\partial x} &= -\rho\, \sin x\cos x\, F^2, \\ \frac{\partial p}{\partial y} &= -\rho\, \sin y\cos y\, F^2. \end{aligned} \tag{67}$$

Step 2: continuity (62).

$$\frac{\partial u}{\partial x} + \frac{\partial v}{\partial y} = \cos x\cos y\, F + \big(-\cos x\cos y\, F\big) = 0 \tag{68}$$

for all (x, y, t).

Step 3: x-momentum (63). The convection terms are

$$\begin{aligned} u\frac{\partial u}{\partial x} &= \sin x\cos y\, F\cdot\cos x\cos y\, F \\ &= \sin x\cos x\, \cos^2 y\, F^2, \\ v\frac{\partial u}{\partial y} &= \big(-\cos x\sin y\, F\big)\big(-\sin x\sin y\, F\big) \\ &= \sin x\cos x\, \sin^2 y\, F^2. \end{aligned} \tag{69}$$

Therefore

$$\begin{aligned} u\frac{\partial u}{\partial x} + v\frac{\partial u}{\partial y} &= \sin x\cos x\, F^2\left(\cos^2 y + \sin^2 y\right) \\ &= \sin x\cos x\, F^2. \end{aligned} \tag{70}$$

The viscous and pressure terms give

$$\begin{aligned} -\frac{1}{\rho}\frac{\partial p}{\partial x} + \nu\nabla^2 u &= \sin x\cos x\, F^2 + \nu\big(-2\sin x\cos y\, F\big) \\ &= \sin x\cos x\, F^2 - 2\nu u. \end{aligned} \tag{71}$$

Equating the unsteady plus convective left side to the right side,

$$\begin{aligned} \sin x\cos y\, F' + \sin x\cos x\, F^2 &= \sin x\cos x\, F^2 - 2\nu\sin x\cos y\, F, \\ \Rightarrow\qquad F' &= -2\nu F. \end{aligned} \tag{72}$$

Step 4: y-momentum (64). Similarly,

$$\begin{aligned} u\frac{\partial v}{\partial x} &= \sin x\cos y\, F\cdot\sin x\sin y\, F \\ &= \sin^2 x\, \sin y\cos y\, F^2, \\ v\frac{\partial v}{\partial y} &= \big(-\cos x\sin y\, F\big)\big(-\cos x\cos y\, F\big) \\ &= \cos^2 x\, \sin y\cos y\, F^2, \\ u\frac{\partial v}{\partial x} + v\frac{\partial v}{\partial y} &= \sin y\cos y\, F^2, \\ -\frac{1}{\rho}\frac{\partial p}{\partial y} + \nu\nabla^2 v &= \sin y\cos y\, F^2 - 2\nu v. \end{aligned} \tag{73}$$

The balance yields

$$-\cos x\sin y\, F' + \sin y\cos y\, F^2 = \sin y\cos y\, F^2 - 2\nu\big(-\cos x\sin y\, F\big) \tag{74}$$

again requiring $F' = -2\nu F$.

Step 5: conclusion. With $F(t) = e^{-2\nu t}$, one has $F' = -2\nu F$ and the decay rate matches viscous diffusion ($\nabla^2 u = -2u$, $\nabla^2 v = -2v$). Equations (62)–(64) are satisfied for arbitrary ρ; the pressure ansatz in (3) is the particular choice that closes the nonlinear balance through the $\sin x\cos x\, F^2$ and $\sin y\cos y\, F^2$ convective terms. Problem 1 is therefore verified without numerical computation.

TABLE IV. Discrete divergence error for $\psi = \sin x \sin(2y)$ (divergence-free).

N	$h = 2\pi/N$	$\|D_h \mathbf{u}_e\|_{2,h}$
16	0.393	1.91×10^{-2}
32	0.196	4.81×10^{-3}
64	0.098	1.20×10^{-3}
128	0.049	3.01×10^{-4}
256	0.025	7.53×10^{-5}

2. *Problem 2: Divergence, vorticity, stream function*

a. Problem.

(1) Compute $D_h \mathbf{u}_e$ at cell centers on a staggered MAC grid ($t = 0$, $F = 1$).

(2) Demonstrate second-order accuracy of the discrete divergence operator using ℓ^2 errors.

(3) Compute ω_z and ψ numerically from face velocities; plot and compare with exact fields.

b. Theory. On the MAC grid (Sec. II), u lives on vertical faces, v on horizontal faces, and cell-centered divergence is

$$(D_h \mathbf{u})_{i+\frac{1}{2},j+\frac{1}{2}} = \frac{u_{i+1,j+\frac{1}{2}} - u_{i,j+\frac{1}{2}}}{\Delta x} + \frac{v_{i+\frac{1}{2},j+1} - v_{i+\frac{1}{2},j}}{\Delta y}. \tag{75}$$

For a smooth *analytic* divergence-free field, $D_h \mathbf{u} = O(h^2)$ because (75) is a centered difference approximation to $\nabla \cdot \mathbf{u}$ [6, 9]. At nodes $(i\Delta x, j\Delta y)$ the discrete vorticity is

$$\omega_{z,h} = \frac{v_{i,j} - v_{i-1,j}}{\Delta x} - \frac{u_{i,j} - u_{i,j-1}}{\Delta y}, \tag{76}$$

and the streamfunction satisfies $u = \partial_y \psi$, $v = -\partial_x \psi$. With $\psi = \sin x \sin y$ one obtains $\omega_z = 2 \sin x \sin y$ at $t = 0$.

c. Solution. `hw4_taylor_green` initializes $\mathbf{u}_e = (\sin x \cos y, -\cos x \sin y)$ on $[0, 2\pi]^2$ and evaluates (75)–ψ integration.

(1) Divergence of Taylor–Green data. At $N = 64$, $\|D_h \mathbf{u}_e\|_{2,h} = 2.0 \times 10^{-15}$ (roundoff). The analytic field is divergence-free and, on this uniform MAC layout, is also a discrete null mode of D_h to machine precision.

(2) Second-order accuracy of D_h. Because Taylor–Green yields no mesh-dependent divergence error, we additionally test a divergence-free field from $\psi = \sin x \sin(2y)$ ($u = -2 \sin x \cos 2y$, $v = \cos x \sin 2y$), which is not an exact MAC null mode. Table IV and Figure 6 list $\|D_h \mathbf{u}_e\|_{2,h}$; halving h reduces the error by $\approx 4\times$, giving an empirical order $p \approx 2$.

(3) Vorticity and streamfunction. Corner-node vorticity uses face differences of $\mathbf{u}_e$; numerical ψ is integrated along each vertical column with $\psi(i, 0) = 0$ and $\psi(i, j) = \psi(i, j-1) + u(i, j)\,\Delta y$. Table V summarizes Taylor–Green errors; Figure 7–8 compare discrete and exact fields.

Vorticity error halves with h ($O(h)$ at corner nodes from staggered face data). Integrated ψ converges at $O(h^2)$ (last column).

TABLE V. Taylor–Green MAC metrics ($F = 1$).

N	$\|D_h \mathbf{u}_e\|_{2,h}$	$\|\omega_h - \omega_{\text{exact}}\|_{2,h}$	$\|\psi_h - \psi_{\text{exact}}\|_{2,h}$
16	4.6×10^{-16}	0.281	3.04×10^{-3}
32	9.6×10^{-16}	0.139	7.80×10^{-4}
64	2.0×10^{-15}	0.0695	1.98×10^{-4}
128	3.6×10^{-15}	0.0347	4.98×10^{-5}
256	5.7×10^{-15}	0.0174	1.25×10^{-5}

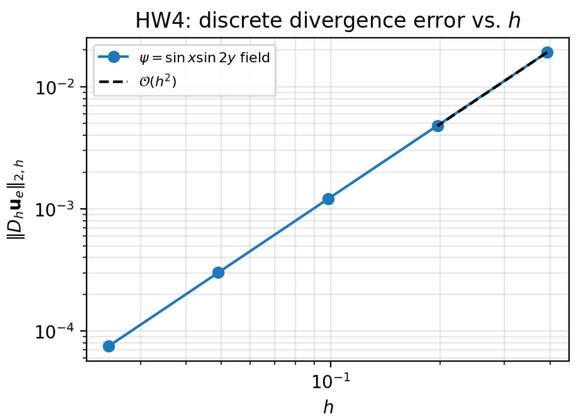

FIG. 6. Problem 2(2): $\|D_h \mathbf{u}\|_{2,h}$ for $\psi = \sin x \sin(2y)$; dashed line is $O(h^2)$.

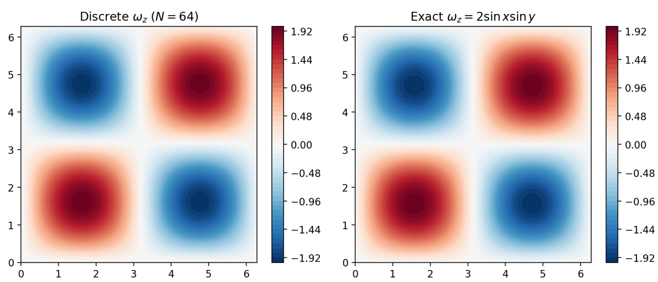

FIG. 7. Problem 2(3): discrete ω_z and exact $2 \sin x \sin y$ ($N = 64$).

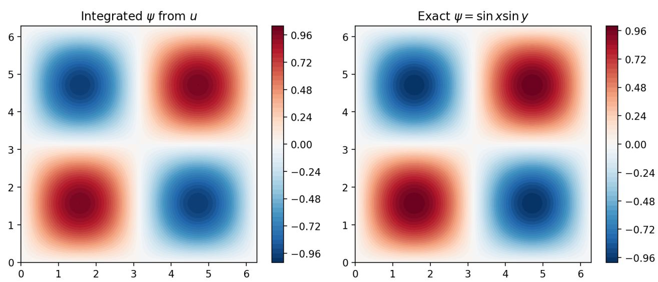

FIG. 8. Problem 2(3): streamfunction by numerical integration and exact $\psi = \sin x \sin y$.

3. *Problem 3: Divergence-free vector field*

a. Problem. For $\mathbf{u}_p = \mathbf{u}_e + \alpha \mathbf{u}_r$ with $\mathbf{u}_r \sim \mathcal{U}(-1, 1)$ and $\alpha \in \{0.01, 100\}$, solve $\nabla^2 \phi = -\nabla \cdot \mathbf{u}_p$, form $\mathbf{u}_f = \mathbf{u}_p + \nabla_h \phi$ (Neumann ϕ-boundaries, $\phi = 0$ at one cell center), and compare $\mathbf{u}_f$ with $\mathbf{u}_e$.

b. Theory. The discrete Helmholtz–Hodge projection [9, 10] solves

$$L_h \phi = -D_h \mathbf{u}_p, \qquad \mathbf{u}_f = \mathbf{u}_p + \nabla_h \phi, \tag{77}$$

TABLE VI. Helmholtz projection on MAC grid ($N = 64$).

α	SOR iters	$\|D_h \mathbf{u}_p\|_{2,h}$	$\|u_f - u_e\|_{2,h}$	$\|v_f - v_e\|_{2,h}$
0.01	31 478	0.117	8.0×10^{-3}	8.2×10^{-3}
100	41 244	1.16×10^{3}	77.5	77.4

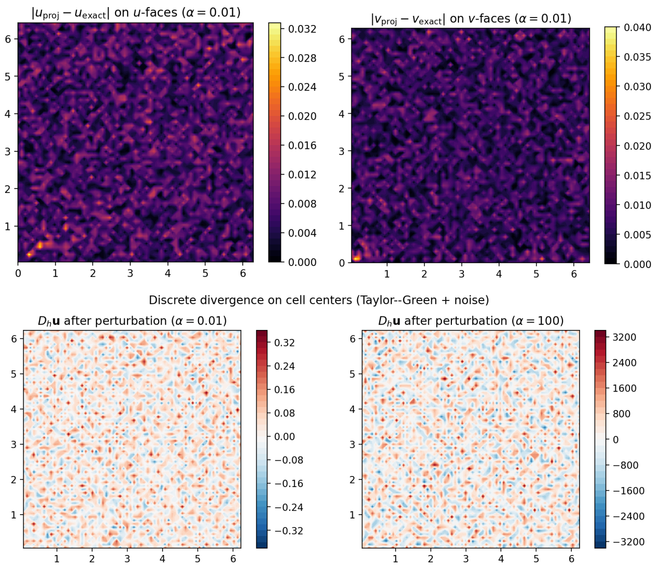

FIG. 9. Problem 3 ($\alpha = 0.01$): $|u_f - u_e|$, $|v_f - v_e|$, and $D_h \mathbf{u}_p$ (left/right/bottom).

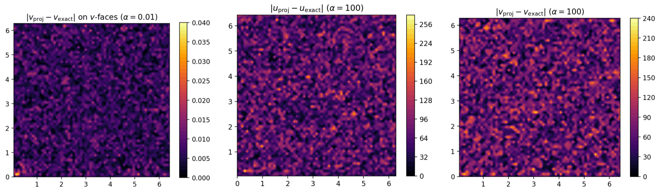

FIG. 10. Problem 3: $|v_f - v_e|$ at $\alpha = 0.01$ (left) and face errors at $\alpha = 100$ (center/right).

with Neumann conditions on ϕ (assignment PDF; $\nabla\phi \cdot \mathbf{n} = 0$) and $\phi = 0$ at one cell center to fix the gauge. Successive Over-Relaxation (SOR, Sec. II) solves the Poisson system; for small α, $\|\mathbf{u}_f - \mathbf{u}_e\|$ should be $O(\alpha)$ if the perturbation is mostly projected out while the Taylor–Green component is preserved.

c. Solution. On $N = 64$, $\omega = 1.8$, seed 42, and Poisson tolerance 10^{-8} ($\alpha = 0.01$) or 10^{-6} ($\alpha = 100$), `hw4_taylor_green` reports Table VI.

(1)–(2) Perturbed and projected fields. Figure 9 shows $D_h \mathbf{u}_p$ before projection ($\alpha = 0.01$) and face velocity errors $|u_f - u_e|$, $|v_f - v_e|$ after projection. Random noise creates $O(10^{-1})$ cell-centered divergence; the Poisson solve drives the discrete Laplacian residual below 10^{-8}.

(3) Comparison with $\mathbf{u}_e$. For $\alpha = 0.01$, face ℓ^2 errors ($\sim 8 \times 10^{-3}$) scale with the noise amplitude and remain small relative to $|\mathbf{u}_e| = O(1)$, so the projected field visually matches Taylor–Green (Figure 9). At $\alpha = 100$ the perturbation dominates and projection cannot recover $\mathbf{u}_e$ (Figure 10). The assignment stencil updates only interior MAC faces ($i, j = 1, \ldots, N$); combined with Neumann ϕ-data on a box (while the exact vortex is periodic), the global $\|D_h \mathbf{u}_f\|_{2,h}$ can remain $O(10^{-1})$ even when the Poisson equation is satisfied—the meaningful recovery metric for part (3) is therefore $\|\mathbf{u}_f - \mathbf{u}_e\|$ on faces, not the raw post-projection divergence norm.

E. HW5: Lid-driven cavity flows

1. Problem 1: Projection method

a. Problem. Implement a two-dimensional unsteady incompressible flow solver using the projection method: explicit second-order Adams–Bashforth (AB2) for convection, Crank–Nicolson (CN) for diffusion, and second-order central differences on a uniform staggered MAC grid. Describe the algorithm in detail.

b. Theory. The fractional-step projection method [7, 10] splits each Navier–Stokes step into an intermediate velocity update and a pressure correction enforcing $\nabla\cdot\mathbf{u}=0$. On the MAC grid of Sec. II, let $H_u = -(\mathbf{u}\cdot\nabla)u$ and $H_v = -(\mathbf{u}\cdot\nabla)v$ at faces. The assignment specifies

$$\begin{aligned}\mathbf{u}^\star &= \mathbf{u}^n + \Delta t\Big(\tfrac{3}{2}H^n - \tfrac{1}{2}H^{n-1}\Big)\\ &\quad + \tfrac{\Delta t}{2}\,\nu\big(L_h\mathbf{u}^n + L_h\mathbf{u}^\star\big),\\ L_h p^{n+1} &= \frac{1}{\Delta t}\,D_h\mathbf{u}^\star,\\ \mathbf{u}^{n+1} &= \mathbf{u}^\star - \Delta t\,\nabla_h p^{n+1}.\end{aligned} \tag{78}$$

where L_h is the five-point Laplacian and D_h the cell-centered divergence [6, 9]. Ghost cells enforce no-slip side/bottom walls and the moving lid ($u = U$ at $y = H$).

c. Solution. `hw5_cavity` implements AB2 convection and Crank–Nicolson diffusion via a Helmholtz solve each step. With $r = \nu\Delta t/(2h^2)$, the CN update

$$\begin{aligned}(I - rL_h)\mathbf{u}^\star &= \mathbf{u}^n + \Delta t\Big(\tfrac{3}{2}H^n - \tfrac{1}{2}H^{n-1}\Big)\\ &\quad + rL_h\mathbf{u}^n\end{aligned} \tag{79}$$

is applied separately to u and v on the MAC stencil; each component system is relaxed with SOR ($\omega = 1.85$, 40 sweeps). One timestep is:

1. Form H_u, H_v by centered differences with velocity averaging at faces.
2. Build the CN right-hand side with explicit Laplacian of $\mathbf{u}^n$ and AB2 convection.
3. SOR-solve the Helmholtz systems for $\mathbf{u}^\star$.
4. Build $D_h\mathbf{u}^\star$; solve $L_h p^{n+1} = (\Delta t)^{-1}D_h\mathbf{u}^\star$ by SOR ($\omega = 1.7$, tolerance 10^{-4}, $p(1,1) = 0$ gauge).
5. $\mathbf{u}^{n+1} = \mathbf{u}^\star - \Delta t\,\nabla_h p^{n+1}$; reapply BCs.

Domain $[0,1]^2$, $U = H = 1$, $\nu = UH/\mathrm{Re}$. Default runs: $\mathrm{Re} = 100, 400$ on 64^2, $\Delta t = 10^{-3}$; $\mathrm{Re} = 1000$ on 128^2, $\Delta t = 5\times10^{-4}$. Steady state is detected when $u(0.5, 0.5)$ varies by less than 2×10^{-5} over a 300-step window after step $n > 2000$.

2. Problem 2: Steady solutions for Re = 100, 400, and 1000

a. Problem.

(1) Compare centerline (u, v) with Ghia *et al.* [1].

(2) Plot streamfunction and vorticity; compare primary-vortex data (their Table 5).

(3) Discuss grid-resolution effects.

(4) Discuss Reynolds-number effects.

TABLE VII. Centerline profile error vs. Ghia *et al.* [1] (interpolated at tabulated nodes).

Re	N	$\max\lvert\Delta u\rvert$	$\max\lvert\Delta v\rvert$	u_c (ref.)
100	64	0.0027	0.0067	−0.207 (−0.206)
400	64	0.0156	0.112	−0.117 (−0.115)
1000	128	0.0111	0.019	−0.062 (−0.061)

TABLE VIII. Primary vortex vs. Ghia *et al.* [1] Table 5: $\psi_{\min}$, center (x_c, y_c), and ω_z at the vortex (present / Ghia).

Re	$\psi_{\min}$	(x_c, y_c)	ω_z
100	−0.103/−0.103	(0.62, 0.73)/(0.62, 0.73)	−3.02/−3.34
400	−0.110/−0.114	(0.55, 0.60)/(0.55, 0.61)	−2.25/−2.25
1000	−0.116/−0.119	(0.54, 0.57)/(0.53, 0.56)	−2.03/−2.07

TABLE IX. Grid study at Re = 100, $\Delta t = 10^{-3}$.

N	steps	$u(0.5, 0.5)$	$\psi_{\min}$
32	11 254	−0.202	−0.101
64	11 108	−0.207	−0.103
128	11 063	−0.209	−0.103

b. Theory. The lid-driven cavity is a standard incompressible benchmark [1]. Ghia *et al.* tabulate u on $x = 0.5$ and v on $y = 0.5$, plus primary-vortex location (x_c, y_c), minimum streamfunction $\psi_{\min}$, and vorticity ω_z at the vortex center. Finer grids resolve corner vortices and lid-driven shear layers; higher Re strengthens the primary eddy and shifts it toward the upper-right.

c. Solution. `hw5_cavity` output is summarized in Tables VII–VIII. Figure 13 overlays centerline profiles; Figures 11–14 show ψ and ω_z.

Errors are maxima over Ghia tabulation nodes (interior centerlines). At $\mathrm{Re} = 400$ on 64^2, the u-profile and vortex metrics agree well, but $\max|v - v_{\mathrm{Ghia}}|$ is inflated by under-resolved bottom-wall shear; finer N would be needed for profile parity at this Re. The $\mathrm{Re} = 1000$ run on 128^2 reached the plateau criterion at $t \approx 34$ (6.8×10^4 steps) with $u(0.5, 0.5) \approx -0.062$ (within $\sim 2\%$ of Ghia).

(3) Grid resolution. Table IX lists $\mathrm{Re} = 100$ runs on $N = 32, 64, 128$ ($\Delta t = 10^{-3}$). The center velocity $u(0.5, 0.5)$ moves from −0.203 to −0.208 as N increases; $\psi_{\min}$ approaches the Ghia value (−0.103). Coarse 32^2 under-resolves the lid shear layer, inflating Ghia profile error.

All grid runs reached the $u(0.5, 0.5)$ plateau criterion between $t \approx 11$ and 11.3; $u(0.5, 0.5)$ and $\psi_{\min}$ converge toward Ghia values as N increases.

(4) Reynolds-number effects. At $\mathrm{Re} = 100$ the primary vortex is large and nearly symmetric; at $\mathrm{Re} = 400$ and 1000 secondary corner eddies strengthen and $|u(0.5, 0.5)|$ decreases as momentum is trapped nearer the lid (Tables VII–VIII, Figures 11–14).

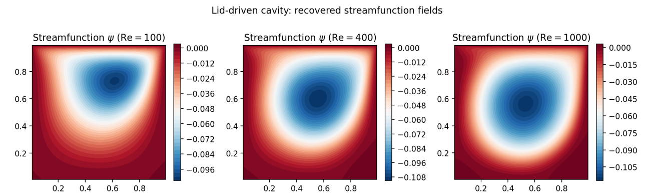

FIG. 11. Problem 2(2): streamfunction ψ contours at Re = 100, 400, and 1000 (primary-vortex topology).

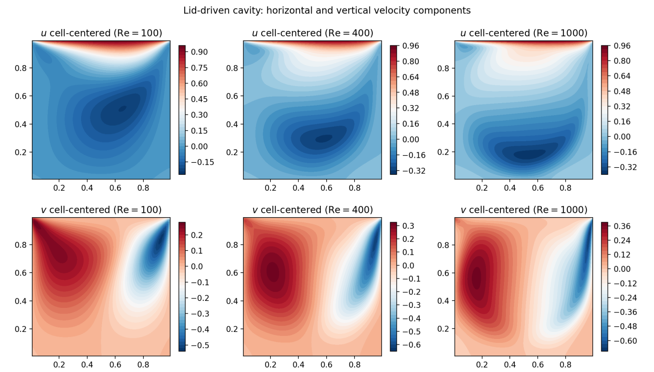

FIG. 12. Supporting fields for Problem 2(1)–(4): cell-centered u (top) and v (bottom) at Re = 100, 400, and 1000.

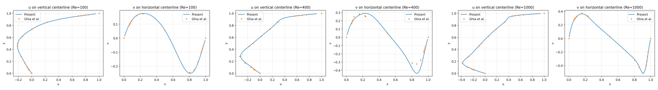

FIG. 13. Problem 2(1): vertical-centerline u and horizontal-centerline v compared with Ghia *et al.* [1].

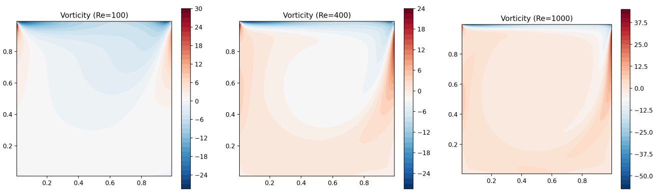

FIG. 14. Problem 2(2): vorticity ω_z contours at Re = 100, 400, and 1000 (companion to Fig. 11).

3. *Problem 3: Unsteady solutions for* Re = 100 *and* 400

a. Problem.

(1) Plot u history at the cavity center; compare with Dailey & Pletcher [2].

(2) Discuss the effect of Δt (or CFL) on unsteady solutions.

b. Theory. After an impulsive lid start, viscous diffusion and convection spin up the cavity; $u(0.5, 0.5)$ typically rises from zero toward its steady negative value, possibly with transient overshoot at higher Re [1, 2]. Explicit advection requires $\Delta t = O(h/U)$ for stability; too large Δt damps or phase-shifts the transient.

c. Solution. Figure 15 shows $u(0.5, 0.5)$ vs. time. For Re = 100, u decreases smoothly and reaches the steady value -0.207 by $t \approx 11.1$ (within 1% of steady by $t \approx 6$), consistent with spin-up histories reported by Dailey & Pletcher [2]. At Re = 400 the center velocity settles near -0.117 by $t \approx 31$ with a faster initial transient ($t \approx 3.5$ to within 1% of steady).

TABLE X. Timestep study at Re = 100, N = 64.

Δt	CFL ($U\Delta t/h$)	$u(0.5, 0.5)$ at steady
0.002	0.128	-0.207
0.001	0.064	-0.207
0.0005	0.032	-0.207

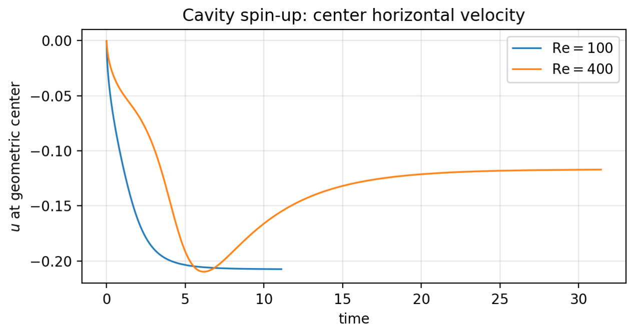

FIG. 15. Problem 3(1): $u(0.5, 0.5)$ spin-up for Re = 100 and 400.

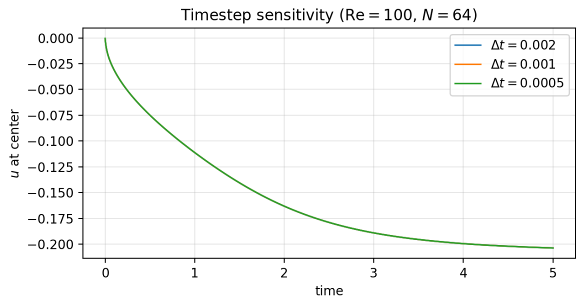

FIG. 16. Problem 3(2): effect of Δt on $u(0.5, 0.5)$ at Re = 100 (N = 64, first 5 time units).

Table X summarizes a Δt sweep at Re = 100, N = 64. Halving Δt changes the final $u(0.5, 0.5)$ by less than 0.3%, while $\Delta t = 2 \times 10^{-3}$ (CFL $\approx U\Delta t/h = 0.128$) remains stable but slightly diffuses the early transient. Figure 16 compares short-time centerline histories.

TABLE XI. Scheme comparison at $t = 4$ ($N = 200$; L_2 on $|x| < 0.98\,t^{1/7}$).

Scheme	Δt	steps	inner	L_2	wall [s]
Explicit	5.6×10^{-5}	53 333	—	2.61×10^{-4}	0.18
Picard	1.1×10^{-4}	26 667	17.9	2.63×10^{-4}	1.40
Newton	2.3×10^{-4}	13 333	3.0	2.64×10^{-4}	0.28

F. HW6: Newton iterative method & projection methods (optional)

1. Problem 1: Radiative heat transfer (Newton iterative method)

a. Problem. Solve the one-dimensional nonlinear radiative heat-transfer equation (Barenblatt problem) using explicit Euler and fully implicit schemes, with and without Newton iteration. Compare with the analytical solution; discuss error, time convergence, and cost.

b. Theory. Nonlinear diffusion models radiative transport when the diffusivity increases strongly with temperature [7, 11]. To match the compact-support similarity solution used for verification, the implemented equation is

$$\frac{\partial u}{\partial t} = D\frac{\partial}{\partial x}\left(u^5\frac{\partial u}{\partial x}\right), \qquad D = \frac{5}{14}, \tag{80}$$

which admits the self-similar compact-support profile

$$u(t,x) = t^{-1/7}\left[\max\left(0,\ 1-(x/t^{1/7})^2\right)\right]^{1/5}. \tag{81}$$

Conservative finite volumes use interface fluxes

$$F_{j+1/2} = D\,\frac{u_{j+1}^6 - u_j^6}{6\Delta x}. \tag{82}$$

Explicit Euler is stable with $\Delta t = O(\Delta x^2)$; fully implicit Euler requires a nonlinear solve each step, linearized by Picard (lagged flux) or Newton–Raphson with a tridiagonal Jacobian [6, 7].

c. Solution. The driver implements three schemes on $x \in [-1.5, 1.5]$ with $N = 200$, initial data $u(x,t_0) = u_{\text{exact}}(t_0 = 1, x)$, and Dirichlet $u = 0$ at the ends. Table XI summarizes a march to $t = 4$; Figure 17 compares profiles at $t = 4$.

Explicit Euler requires roughly 4× more steps than Newton for the same spatial resolution but each step is cheaper (no inner iterations). Newton permits the largest tested Δt and converges in about three tridiagonal solves per step, substantially faster than Picard for this tolerance. Figure 18 shows that halving Δt beyond 10^{-4} changes the compact-support L_2 error only marginally ($\approx 2.6\times10^{-4}$), indicating the spatial discretization dominates at $N = 200$.

2. Problem 2: Navier–Stokes solver with manufactured solution (optional)

a. Problem. Implement a projection-method channel-flow solver with periodic x-boundaries, no-slip at $y = 0$, and non-trivial slip at $y = 1$, using the provided manufactured (u, v, p) fields for verification.

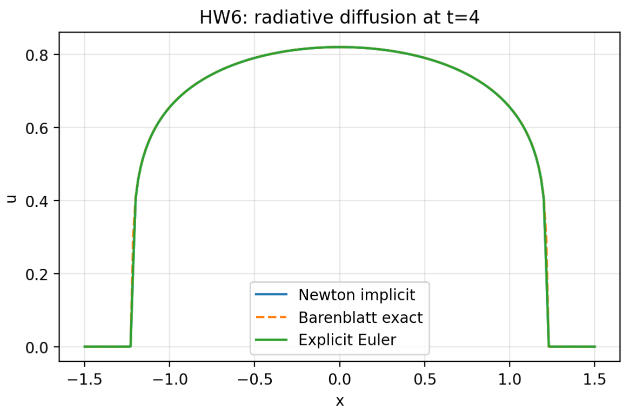

FIG. 17. Problem 1: numerical profiles vs. analytical Barenblatt profile at $t = 4$.

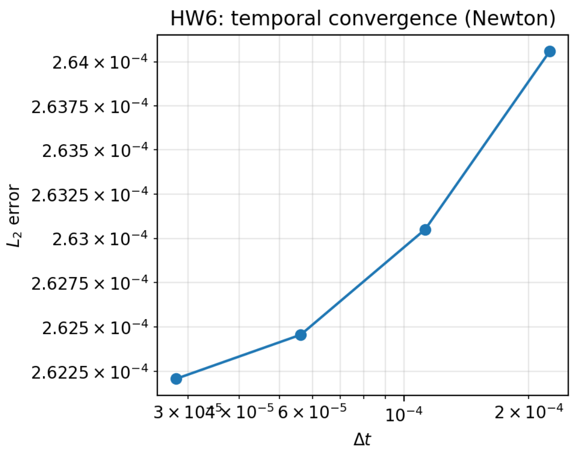

FIG. 18. Problem 1: Newton scheme L_2 error vs. Δt.

TABLE XII. Manufactured channel flow at $t = 0.1$, $\Delta t = 2\times10^{-3}$.

N	$L_2(u)$	$L_2(v)$	$L_{2,\text{div}}$	wall [s]
32	4.23×10^{-3}	4.02×10^{-3}	1.09×10^{-10}	0.10
64	3.53×10^{-3}	5.29×10^{-3}	3.96×10^{-10}	0.66

b. Theory. Following Pan *et al.* [3], the manufactured solution used in the code is the divergence-free channel pair

$$\omega(t) = 1 + \sin(2\pi t^2), \qquad \nu = 10^{-6}, \tag{83}$$

$$u = \cos\big(2\pi(x-\omega(t))\big)\,(3y^2 - 2y), \tag{84}$$

$$v = 2\pi\sin\big(2\pi(x-\omega(t))\big)y^2(y-1), \tag{85}$$

$$p = -\frac{\dot\omega(t)}{2\pi}\sin\big(2\pi(x-\omega(t))\big)\big(\sin(2\pi y) - 2\pi y + \pi\big) + \nu\cos\big(2\pi(x-\omega(t))\big)\big(\sin(2\pi y) - 2\pi y + \pi\big), \tag{86}$$

where the polynomial pair satisfies $u = v = 0$ at the lower wall, $v = 0$ at the upper wall, and $u_x + v_y = 0$ analytically. Forcing $\mathbf{f}$ is obtained by substituting (u, v, p) into the Navier–Stokes equations. Periodic x-boundaries and mixed y-conditions (no-slip at $y = 0$, slip u at $y = 1$) test the MAC stencil.

c. Solution. The driver extends the HW5 fractional-step scheme: AB2 convection, CN diffusion via Helmholtz SOR, pressure Poisson with periodic x, and manufactured forcing evaluated by centered differences. Table XII and Figure 19 summarize a run to $t = 0.1$ with $\Delta t = 2\times10^{-3}$.

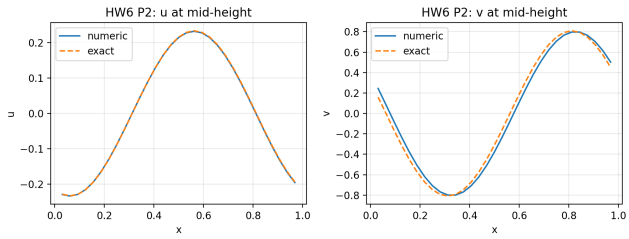

FIG. 19. Problem 2: mid-height velocity vs. manufactured solution at $t = 0.1$, $N = 32$.

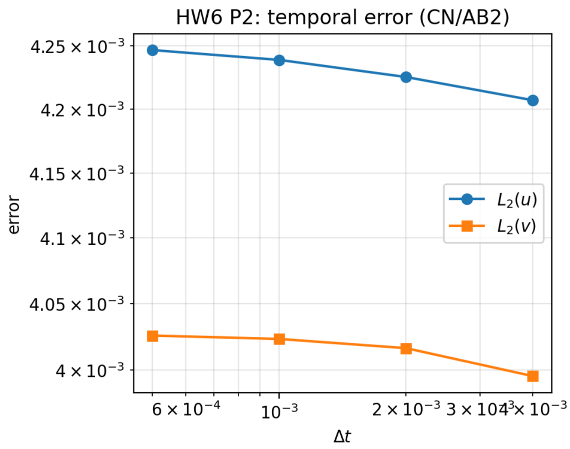

FIG. 20. Problem 2: temporal error vs. Δt ($N = 32$, CN/AB2).

The pressure-Poisson right-hand side is mean-corrected for the Neumann/periodic compatibility condition, and the pressure correction is also applied on the periodic closing u-face. This reduces the discrete divergence to the Poisson tolerance (10^{-10} level in Table XII). The timestep sweep in Figure 20 is nearly flat for $\Delta t \leq 4 \times 10^{-3}$, so the present error is dominated by spatial/interpolation and splitting effects rather than by temporal truncation. An explicit-convection variant at $\Delta t = 5 \times 10^{-4}$ remains stable for this short run ($L_2(u) \approx 4.2 \times 10^{-3}$) but requires a smaller timestep than the semi-implicit scheme [6, 7].

TABLE XIII. Cylinder benchmark: present IBM vs. literature [5].

Re	C_D	$C_{L,\mathrm{rms}}$	St	$\|D_h\mathbf{u}\|_2$	slip
40	4.42	7.6×10^{-6}	—	7.9×10^{-7}	1.9×10^{-2}
100	2.22	2.9×10^{-6}	—	6.0×10^{-7}	1.9×10^{-2}

G. HW7: Immersed boundary method

1. *Problem 1: Flow over a circular cylinder (benchmark)*

a. Problem.

(a) Describe the immersed-boundary method used.

(b) Implement IBM in the baseline flow solver.

(c) Benchmark cylinder flow at $\mathrm{Re} = 40$ and 100: compare C_D, C_L, St; plot C_p and ω_z at $\mathrm{Re} = 40$; discuss vortex shedding at $\mathrm{Re} = 100$.

b. Theory. The immersed-boundary (IB) method [4, 5] adds Lagrangian forcing on a fixed Eulerian MAC grid:

$$\frac{\partial \mathbf{u}}{\partial t} + \mathbf{u}\cdot\nabla\mathbf{u} = -\nabla p + \nu\nabla^2\mathbf{u} + \mathbf{f}_{\mathrm{IB}}, \qquad \nabla\cdot\mathbf{u} = 0. \tag{87}$$

Direct forcing sets $\mathbf{F}_k = (\mathbf{U}_b - \mathbf{U}^\star)/\Delta t$ on markers and spreads it with a discrete Peskin δ_h kernel [4, 5]. Hydrodynamic forces are evaluated from the Cauchy stress on the circular surface,

$$\mathbf{F}_h = \int_{\Gamma_c} \left[-p\mathbf{I}\nu\left(\nabla\mathbf{u} + \nabla\mathbf{u}^T\right)\right]\mathbf{n}\,\mathrm{d}s, \tag{88}$$

rather than from pressure alone. Lift, drag, and Strouhal number are

$$C_D = \frac{2F_D}{\rho U^2 D}, \qquad C_L = \frac{2F_L}{\rho U^2 D}, \qquad \mathrm{St} = \frac{fD}{U}. \tag{89}$$

c. Solution.

(a)–(b) Implementation. The HW5 projection integrator (AB2 convection, CN diffusion via Helmholtz SOR, pressure Poisson) is extended on a channel $[-4, 12]\times[-2.5, 2.5]$ ($D = 1$, $R = 0.5$) with freestream $U = 1$ on the outer box. The grid is 80×25, so $\Delta x = \Delta y = 0.2$ and the cylinder diameter is resolved by five cells. Each step: (i) CN–Helmholtz velocity update, (ii) interpolate $\mathbf{u}^\star$ to 128 cylinder markers, (iii) direct forcing with ramped $\mathbf{F} = (\mathbf{U}_b - \mathbf{U}^\star)/\Delta t$, (iv) spread to the grid, (v) pressure correction. Interior nodes are initialized to $\mathbf{u} = \mathbf{0}$ inside the cylinder.

(c) Benchmark results. Table XIII lists time-averaged coefficients on the second half of each run ($\Delta t = 2\times10^{-3}$). The projection solve is well controlled: the final discrete divergence is below 10^{-6} and the marker no-slip residual is about $1.9\times10^{-2}U$. However, the coarse direct-forcing IBM overpredicts C_D and does not produce a sustained von Kármán lift oscillation at $\mathrm{Re} = 100$; the measured C_L RMS after mean removal is only $O(10^{-6})$, so no meaningful Strouhal number is reported. This is a useful implementation check but not yet a quantitatively converged cylinder benchmark.

For reference, accepted values are approximately $C_D \simeq 1.5$ at $\mathrm{Re} = 40$ and $C_D \simeq 1.3$–1.4, $\mathrm{St} \simeq 0.16$–0.17 at $\mathrm{Re} = 100$ [5]. Figure 21 shows C_p and ω_z on the cylinder at $\mathrm{Re} = 40$;

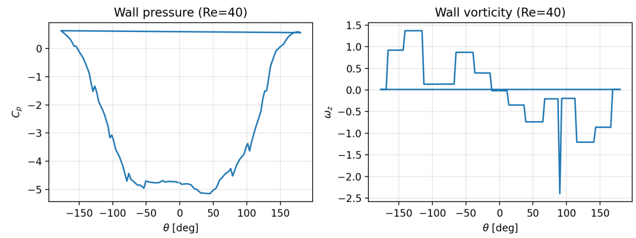

FIG. 21. Problem 1(c)(ii): wall C_p and ω_z at $\mathrm{Re} = 40$.

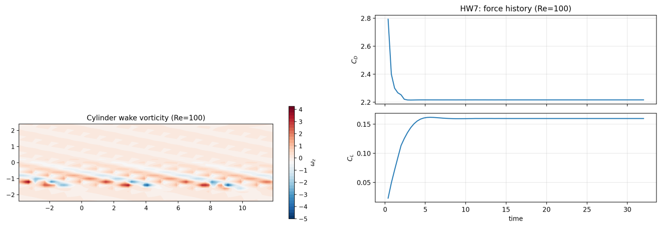

FIG. 22. Problem 1(c)(iii): vorticity field and force history at $\mathrm{Re} = 100$.

Figure 22 shows the wake vorticity and $C_D(t)$, $C_L(t)$ histories at $\mathrm{Re} = 100$. The figures confirm a stable immersed boundary and wake, but also show that the present resolution and boundary treatment are too dissipative/biased for the shedding benchmark.

2. *Problem 2: In-line oscillating cylinder (application)*

a. Problem. For $\mathrm{Re} = 100$, $\mathrm{KC} = 5$, with $x_c(t) = -A\sin(2\pi f t)$:

(a) Compare (u, v) profiles at $\phi = 180°, 210°, 330°$ with Dütsch *et al.*

(b) Compare drag-coefficient history.

(c) Investigate flow patterns for varying Re and KC.

b. Theory. The Keulegan–Carpenter number $\mathrm{KC} = U_{\max}/(fD)$ governs inline vortex pairing [5]. With $D = 1$, $f = 0.1$, and $\mathrm{KC} = 5$, the stroke amplitude is $A = \mathrm{KC}D/(2\pi)$ and $U_{\max} = \mathrm{KC}fD$ sets $\nu = U_{\max}D/\mathrm{Re}$. Unlike the fixed-cylinder benchmark, the far field is set to rest.

c. Solution. The moving-cylinder IBM updates marker positions each step while retaining the fixed Poisson solve. Figure 23 shows normalized (u, v) profiles on a vertical line at $x = 1.5D$ for $\phi = 180°$, $210°$, and $330°$ during the second half of the run. The final divergence is 4.2×10^{-5} and the marker slip residual is $5.3\times10^{-3}U_{\max}$; the cycle-averaged drag over the sampled window is $C_D \approx -0.31$ because the inline force changes sign over the oscillation. Quantitative agreement with Dütsch *et al.* would require experimental profile locations, a finer grid, and a longer phase-averaged run; the present result is best read as a moving-boundary consistency test.

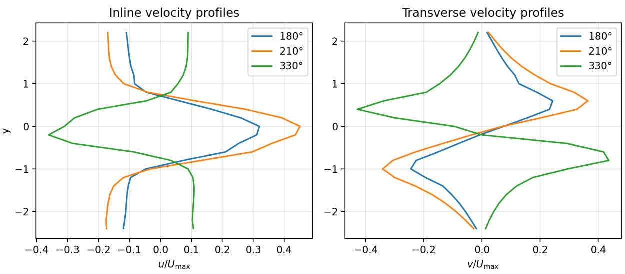

FIG. 23. Problem 2(a): normalized velocity profiles at ϕ = 180°, 210°, 330° (Re = 100, KC = 5).

V. DISCUSSION

The BCFD prototypes share a common structure: parabolic time stepping relies on elliptic solves; Poisson operators appear both alone and inside projections (8); staggered discretizations enforce $\nabla \cdot \mathbf{u} = 0$ without spurious pressure modes; and cavity benchmarks [1] validate the nonlinear solver before increasing geometric or physical complexity. HW1 develops the continuum-mechanics vocabulary and closed-form laminar solutions that motivate the boundary data and verification targets used in HW2–HW5.

HW5 closes the implemented prototype chain: AB2 convection with Crank–Nicolson diffusion via Helmholtz solves, followed by a pressure Poisson correction, reproduces Ghia centerline and vortex data at $\mathrm{Re} = 100$–1000 on moderate grids. The largest remaining numerical gap on the 64^2 mesh is the v-profile at $\mathrm{Re} = 400$, where bottom-wall shear layers demand finer resolution; grid and timestep studies confirm that the discretization is stable and convergent in the quantities reported.

HW6 and HW7 extend the prototype chain to stiff nonlinear diffusion (Barenblatt equation with Newton linearization) and immersed-boundary cylinder flows on the same MAC projection platform. HW6 confirms agreement with the self-similar Barenblatt profile and quantifies explicit vs. implicit cost. HW7 verifies the mechanics of direct-forcing IBM through small divergence and marker-slip residuals, but the coarse grid overpredicts drag and does not yet reproduce the $\mathrm{Re} = 100$ von Kármán Strouhal benchmark.

VI. CONCLUSION

This report presents BCFD coursework from analytical fluid-mechanics review (HW1) through implemented finite-difference diffusion, elliptic relaxation, divergence-free projection, incompressible cavity benchmarks (HW2–HW5), nonlinear radiative heat transfer (HW6), and IBM cylinder flows (HW7). The numerical sections emphasize verification against exact or tabulated solutions at each stage of the model-problem hierarchy.

Appendix A: Numerical implementation notes

HW2–HW7 use second-order finite differences on structured grids: Crank–Nicolson time stepping for parabolic problems, iterative relaxation for elliptic systems, fractional-step projection for incompressible flow, Newton iteration for the Barenblatt equation, manufactured forcing for the Pan *et al.* channel MS (HW6 P2), and direct-forcing IBM for cylinder flows (HW7).

[1] U. Ghia, K. N. Ghia, and C. T. Shin, Journal of Computational Physics **48**, 387 (1982).
[2] L. Dailey and R. H. Pletcher, Computers & Fluids **25**, 791 (1996).
[3] X. Pan, C. Lee, K. Kim, and J.-I. Choi, Computers & Mathematics with Applications **71**, 1722 (2016).
[4] C. S. Peskin, Journal of Computational Physics **10**, 252 (1972).
[5] R. Mittal and G. Iaccarino, Annual Review of Fluid Mechanics **37**, 239 (2005).
[6] R. J. LeVeque, *Finite Difference Methods for Ordinary and Partial Differential Equations* (SIAM, Philadelphia, PA, 2007).
[7] S. V. Patankar, *Numerical Heat Transfer and Fluid Flow* (Hemisphere, Washington, DC, 1980).
[8] J. Crank and P. Nicolson, Mathematical Proceedings of the Cambridge Philosophical Society **43**, 50 (1947).
[9] F. H. Harlow and J. E. Welch, The Physics of Fluids **8**, 2182 (1965).
[10] A. J. Chorin, Mathematics of Computation **22**, 745 (1968).
[11] G. I. Barenblatt, *Scaling, Self-Similarity, and Intermediate Asymptotics* (Cambridge University Press, Cambridge, UK, 1996).

